2. Axelsson B, Msaki P, Israelsson A. Subtraction of Compton-scattered photons in single photon emission computerized tomography. *J Nucl Med* 1984;25:490–494.
3. Jaszczak R, Greer KL, Floyd CE, Harris CC, Coleman RE. Improved SPECT quantification using compensation for scattered photons. *J Nucl Med* 1984;25:893–900.
4. Floyd CE, Jaszczak RJ, Greer KL, Coleman RE. Deconvolution of Compton scatter in SPECT. *J Nucl Med* 1985;26:403–408.
5. Halama JR, Henkin RE, Friend LE. Gamma camera radionuclide images: improved contrast with energy-weighted acquisition. *Radiology* 1988;169:533–538.
6. Msaki P, Axelsson, B, Dahl CM, Larsson SA. A generalized scatter correction technique in SPECT using point scatter distribution functions. *J Nucl Med* 1987;28: 1861–1869.
7. Koral KF, Wang X, Rogers WL, Clinthorne NH, Wang X. SPECT Compton-scattering correction by analysis of energy spectra. *J Nucl Med* 1988;29:195–202.
8. Gilardi MC, Bettinardi V, Todd-Pokropek A, Milanesi L, Fazio F. Assessment and comparison of three scatter correction techniques in single photon emission computed tomography. *J Nucl Med* 1988;29:1971–1979.
9. Gagnon D, Todd-Pokropek A, Arsenault A, Dupras G. Introduction to holospectral imaging in nuclear medicine for scatter subtraction. *IEEE Trans Med Imaging* 1989;8:245–250.
10. Ljungberg M, Strand SE. Scatter and attenuation correction in SPECT using density maps and Monte Carlo simulated scatter functions. *J Nucl Med* 1990;31:1560–1567.
11. King MA, Hademenos GJ, Glick SJ. A dual-photopeak window method for scatter correction. *J Nucl Med* 1992;33:605–612.
12. Maor D, Berlad G, Chrem Y, Voil A, Todd-Pokropek A. Klein-Nishina based energy factors for Compton-free imaging (CFI) [Abstract]. *J Nucl Med* 1991;32:1000.
13. Ichihara T, Ogawa K, Motomura N, Kubo A, Hashimoto S. Compton scatter compensation using the triple energy window method for single and dual isotope SPECT. *J Nucl Med* 1993;34:2216–2221.
14. Buvat I, Rodriguez-Villafuerte M, Todd-Pokropek A, Benali H, Di Paola R. Comparative assessment of nine scatter correction methods based on spectral analysis using Monte Carlo simulations. *J Nucl Med* 1995;36:1476–1488.
15. Mas J, Hannequin P, Ben Younes R, Bellaton B, Bidet R. Scatter correction in planar imaging and SPECT by constrained factor analysis of dynamic structures (FADS). *Phys Med Biol* 1990;35:1451–1465.
16. Buvat I, Benali H, Frouin F, et al. Target apex-seeking in factor analysis of medical image sequences. *Phys Med Biol* 1993;28:123–138.
17. Weisberg S. *Applied linear regression*. New York: Wiley; 1985:124.
18. Hocking RR. The analysis and selection of variables in linear regression. *Biometrics* 1976;32:1–49.
19. Thompson M. Selection of variables in multiple regression. Part I: a review and evaluation. *Int Stat Rev* 1978;46:1–19.
20. Thompson M. Selection of variables in multiple regression. Part II: chosen procedures, computation and examples. *Int Stat Rev* 1978;46:129–146.
21. Beck JW, Jaszczak RJ, Coleman RE, Starmer CF, Nolte LW. Analysis of SPECT including scatter and attenuation using sophisticated Monte Carlo modeling methods. *IEEE Trans Nucl Sci* 1982;NS-29:506–511.
22. Floyd CE, Jaszczak RJ, Harris CC, Coleman RE. Energy and spatial distribution of multiple order Compton scatter in SPECT: a Monte Carlo investigation. *Phys Med Biol* 1984;29:1217–1230.
23. Floyd CE, Jaszczak RJ, Harris CC, Greer KL, Coleman RE. Monte Carlo evaluation of Compton scatter subtraction in single photon emission computed tomography. *Med Phys* 1985;12:776–778.
24. Ben Younes R, Mas J, Pousse A, Bidet R. Compton scatter correction by spectral iterative deconvolution [Abstract]. *Eur J Nucl Med* 1991;18:541.
25. Wang X, Koral KF. A regularized deconvolution-fitting method for Compton-scatter correction in SPECT. *IEEE Trans Med Imaging* 1992;11:351–360.
26. Palm R, Iemma AF. Quelques alternatives à la régression classique dans le cas de la colinéarité. *Rev Stat Appl* 1995;43:5–33.

A Comparison of 180° and 360° Acquisition for Attenuation-Compensated Thallium-201 SPECT Images

Karen J. LaCroix, Benjamin M.W. Tsui and Bruce H. Hasegawa

Department of Biomedical Engineering and Department of Radiology, The University of North Carolina at Chapel Hill, Chapel Hill, North Carolina; and The Bioengineering Graduate Group and Department of Radiology, University of California, San Francisco, California

This study compared attenuation compensated, myocardial SPECT images reconstructed from 180° and 360° data to determine if either data acquisition method might yield improved image quality. Specifically, this study analyzed how the use of either 180° or 360° data affects: (a) the relative count density distribution, (b) defect contrast and (c) level of statistical noise in the left ventricular (LV) wall in the reconstructed SPECT images. **Methods:** Using the three-dimensional MCAT phantom simulating ^{201}Tl uptake in the upper torso and the SIMSET Monte Carlo code, noise-free projection datasets for both 180° (45° LPO to 45° RAO) and 360° acquisition were generated with the effects of nonuniform attenuation, collimator-detector response and scatter. In addition, low-noise experimental phantom data were acquired over 180° and 360°. Assuming the same total acquisition time, four sets of noisy projection data were simulated from scaled noise-free, simulated data for the following acquisitions: (a) 180° and (b) 360° data acquired on a 90° dual-detector system and (c) 180° and (d) 360° data acquired on a 120° triple-detector system. For each of the four acquisition schemes, 400 realizations of noisy projection data were generated, and the normalized s.d. in the reconstructed images was calculated for five ROIs in the LV wall. Images were reconstructed with nonuniform attenuation compensation using ML-EM algorithm for 25, 50 and 75 iterations. **Results:** Both the simulated noise-free and experimental low-noise images reconstructed from 180° and 360° data showed nearly identical count densities and defect contrasts in the LV wall. For the 90° dual-detector system, 180° images showed less noise, while for the 120° triple-detector system, 360° showed less noise; however, these differences in noise level were extremely small after a smoothing filter was applied. The 180° images acquired with the 90° dual-detector system showed the same noise level as the 360° images acquired with the 120° triple-detector system, so neither system geometry had an advantage with respect to reduced noise in the SPECT images. **Conclusion:** When nonuniform attenuation compensation is included in the reconstruction, the count density in the LV wall is nearly identical for 180° and 360° SPECT images, and the 90° dual-detector and 120° triple-detector SPECT systems produced similar SPECT images for the same total acquisition time.

Key Words: SPECT; attenuation compensation; thallium-201 perfusion agents; cardiac simulation study

J Nucl Med 1998; 39:562–574

Many previous studies have compared ^{201}Tl SPECT images reconstructed from data acquired over 180°, specifically the 45° right anterior oblique (RAO) to the 45° left posterior oblique (LPO) arc, to images reconstructed from data acquired over 360° using, for reconstruction, the filtered backprojection method (*1–6*). These studies have shown that the images reconstructed from 180° data generally have better contrast and spatial resolution in the left anterior region of the patient (where

Received Dec. 2, 1996; revision accepted May 8, 1997.

For correspondence or reprints contact: Karen J. LaCroix, PhD, Dept. of Biomedical Engineering, CB #7575, 152 MacNider, The University of North Carolina at Chapel Hill, Chapel Hill, NC 27599.

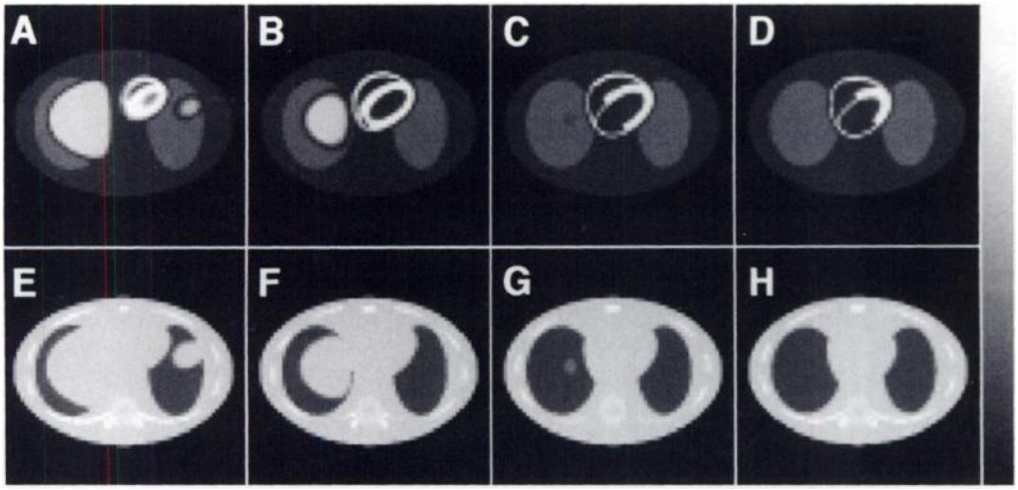

FIGURE 1. (A-D) The distribution of ^{201}Tl uptake and (E-H) the corresponding distribution of attenuation coefficients for several transaxial, cardiac slices of the MCAT phantom. (A,E) The inferior-most slice of this group is on the left with progression to (D,H) the superior-most slice on the right. At this slice thickness (0.625 cm), there are 14 transaxial slices that contain myocardium; only four of those slices are shown here.

the left ventricle is located) than the images reconstructed from 360° data. This observation has led some researchers (*2,6*) to recommend 180° data acquisition over 360° data acquisition for cardiac SPECT images. However, the same studies also have shown that images reconstructed from 180° data generally have more artifacts and spatial distortion as compared to images reconstructed from 360° data, especially towards the basal region of the myocardium. This observation has led other researchers (*1,3,4*) to recommend 360° data acquisition over 180° data acquisition. Regardless of the interpretation of the results, it is clear from these studies that the images reconstructed from 180° and 360° data exhibit different distributions of count density in the left ventricular (LV) wall. Simulations by Knesaurek et al. (*5*) showed that the differences in count density between the 180° and 360° images largely were due to the effects of nonuniform attenuation, which had not been compensated for in the reconstruction. Furthermore, a simulation study of ^{99m}Tc SPECT images, where there was very high radionuclide uptake in the liver, showed that iterative reconstruction with nonuniform attenuation compensation nearly eliminated severe artifacts in 180° images, producing similar 180° and 360° images (*7*).

A previous simulation study (*8*) compared ^{201}Tl SPECT images reconstructed from 180° and 360° data, where the images were reconstructed iteratively with compensation for nonuniform attenuation using the maximum likelihood-expectation maximization (ML-EM) algorithm (*9,10*). The images reconstructed with attenuation compensation, unlike the images reconstructed without attenuation compensation, had nearly identical distributions of count density in the LV wall. The attenuation compensation appeared to have reduced the artifacts and distortion in the 180° images but also appeared to have reduced the apparent gain in contrast and resolution traditionally associated with 180° images. The only differences between the 180° and 360° images were observed in the right, posterior region of the patient—a region not generally of interest for the assessment of LV myocardial perfusion. This study went on to state that for a single-detector SPECT system, given the same total acquisition time for the 180° and 360° data, the 180° images had less noise in the LV wall.

The previous study had several major limitations that are the basis for the study described in this paper. First, the phantom used in the previous study modeled a smaller than average patient torso size. Therefore, there was still a question as to whether or not greater differences would be observed between the 180° and 360° images for a larger size patient where the effects of nonuniform attenuation on the reconstructed images, if any, would be greater (more noticeable). Second, the study only compared the noise level in the reconstructed images, assuming the data were acquired on a single-detector SPECT system and did not study the relative noise levels for data acquired on multidetector SPECT systems. Third, the results needed some validation with experimental data.

The purpose of this study was to compare images iteratively reconstructed with nonuniform attenuation compensation from 180° and 360° data, where the data were acquired on a multidetector system. This study has two parts. In the first part, a comparison of the reconstructed count density in noise-free 180° and 360° images revealed the extent of underlying, systematic differences between the 180° and 360° images, independent of differences due to statistical noise. Completely noise-free images were generated using simulated data. In addition, to validate the results of the simulation, this analysis was performed using low-noise ^{201}Tl data obtained experimentally using a physical phantom. In the second part of this study, an analysis of noisy 180° and 360° images revealed the extent of differences in the noise level between 180° and 360° images. This analysis was performed using simulated noisy data.

MATERIALS AND METHODS

Simulated Data

All simulated data for this study were generated using the three-dimensional Mathematical CArdiac-Torso phantom (MCAT) developed at the University of North Carolina at Chapel Hill (*11*). For several transaxial slices through the LV wall of the MCAT phantom, Figure 1 shows the relative distribution of ^{201}Tl and the corresponding distribution of attenuation coefficients. The attenuation coefficient values were calculated assuming a photon energy of 72 keV, the approximate average energy of ^{201}Tl photon emissions. Assuming a patient at stress at 10 min after injection, the relative uptake ratios of ^{201}Tl in the torso organs were 43, 19, 6 and 2 for the myocardium, liver, lung and body, respectively. The "body" uptake is the background uptake and includes the muscle and bone tissues. The exact uptake of ^{201}Tl in human organs varies among patients. The uptake ratios used in this study were based on exact measurements of ^{201}Tl organ uptake at 10 min after injection in a goat, the animal closest to a human for which such measurements have been made (*12*). A visual comparison of simulated, reconstructed SPECT images to ^{201}Tl stress patient images was made, and it was concluded that the goat-based uptake ratios provide a reasonable uptake model for many patients, although due to variations in lung and liver uptake in humans, the goat-based uptake ratios are more accurate for some patients than others.

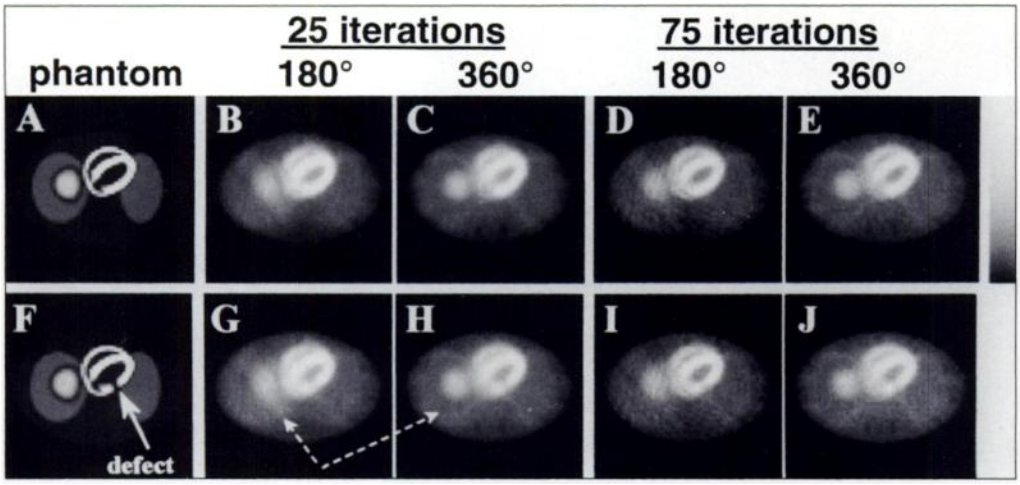

FIGURE 2. (B,D) Images reconstructed from 180° and (C,E) 360° noise-free data along with (A) the corresponding MCAT phantom slice modeling normal ^{201}Tl uptake in the myocardium. For the same slice as A–E, images reconstructed from (G,I) 180° and (H,J) 360° noise-free data along with (F) the corresponding MCAT phantom slice modeling a cold defect in the basal-lateral LV wall.

Cold defects in the LV wall were simulated in the MCAT phantom as three-dimensional, isotropic regions of decreased activity, Gaussian in profile. At the defect center, the activity is the same as the "body" tissue. The FWHM of each defect is approximately 1.65 cm, which is slightly greater than the 1.3-cm width of the LV wall, so each defect is transmural. For this study, defects were simulated separately at two different locations. The "anterior" defect is located in the anterior wall of the LV near the apex, and the "basal" defect is located in the lateral wall of the LV near the base. The defect centers are located in different transaxial slices, with the slice containing the anterior defect being superior to the slice containing the basal defect by 1.875 cm (3 slices).

The phantom models a medium-large male patient whose elliptically shaped torso has a 36-cm long axis (lateral width) and 24-cm short axis. The phantom was stored in a 64 × 64 × 64 array with a pixel size and slice thickness of 0.625 cm. This results in a 40-cm field of view in each dimension.

A Monte Carlo simulation, using the Simulation System for Emission Tomography (SIMSET) code (*13*), was used to generate emission projection data with nonuniform attenuation, collimator-detector response and scatter. The Monte Carlo data were simulated for a parallel-hole, LEGP collimator with a hole length of 4.1 cm and a circular-hole diameter of 0.26 cm. The simulated energy window was centered at 72 keV with a 30% width. All projection data were simulated into 64 bins, 41 slices and either 64 or 128 views for either 180° or 360° data, respectively. The radius of rotation was 22.5 cm, and both the slice thickness and bin width were 0.625 cm.

The "noise-free" emission data obtained from the Monte Carlo simulation not truly noise-free but were relatively noise-free. An extremely long acquisition time was simulated, and the resulting simulated emission data has a negligible level of statistical noise compared with the level of statistical noise in typical SPECT emission data.

Noisy data were generated by simulating Poisson noise in scaled noise-free data. The noise-free data were scaled assuming: (a) the same total acquisition time (variable time per view) for all sets of data and (b) assuming approximately 150,000 counts in the 180° data acquired over 90° with a dual-detector system for the 6.25-mm slice shown in Figure 2A.

The attenuation map for the simulated data was the MCAT phantom attenuation coefficient distribution, blurred by a Gaussian filter to produce an attenuation map with approximately the same spatial resolution as the modeled detector. This blurring is necessary because it has been shown that if the attenuation map has much better spatial resolution than that of the emission data, unwanted artifacts will appear in the reconstructed images (*14,15*). It has been shown that, with a judicious choice of radionuclides and proper collimation at the transmission source and detector, the amount of scatter in the transmission data is negligible (*16*). Therefore, the use of an attenuation map with narrow-beam attenuation coefficients is a reasonably accurate approximation.

Experimental Data

The experimental data were acquired with an anthropomorphic torso phantom (Data Spectrum Corp., Hillsborough, NC) which models a patient with a lateral width of approximately 38 cm and an anterior-posterior width of approximately 28 cm. In addition to the main torso compartment, the phantom has separate compartments for the myocardium, lungs and liver-stomach. The phantom was filled with approximately 4.77 mCi ^{201}Tl. No defects were simulated in the myocardium compartment. The relative uptake ratios of ^{201}Tl in the phantom organ compartments are approximately 43, 19, 1 and 2 for the myocardium, liver-stomach, lung and body compartments, respectively. These are approximately the same uptake ratios used in the MCAT phantom, with the exception of the lung. In the experimental data, the lung uptake was lower than in the simulated MCAT phantom. This lower lung uptake often is seen in patient ^{201}Tl studies. Since the uptake in the lungs is very low compared to the myocardium in both the simulated and experimental data, the difference in lung uptake did not affect the results of this study.

Emission projections were acquired on a dual-head SPECT system. Each head acquired a full 360° dataset over 128 views using a 20-cm radius of rotation. These sets were added to give a total acquisition time per view of 80 sec. The 180° (45° RAO to 45° LPO) data over 64 views were extracted from the 360° dataset. Data were acquired using a LEGP collimator with parallel hexagonal holes of 3.5 cm length and 0.18 cm flat-to-flat width. The energy window was centered at 75 keV with a 32% window width. The bin size and slice thickness were 6 mm.

Transmission projections also were acquired on the dual-head SPECT system, using a ^{153}Gd scanning line source. Each head acquired a full 360° dataset over 128 views using a 20-cm radius of rotation. From the transmission data, an attenuation map, at the energy of ^{153}Gd, was reconstructed using filtered backprojection and subsequently scaled to yield an attenuation map for ^{201}Tl. The scaling factor was the ratio of the attenuation coefficient of water at 72 keV (approximate mean energy of ^{201}Tl photons) to the attenuation coefficient of water at 100 keV (approximate mean energy of ^{153}Gd photons). Finally, the attenuation map was blurred with the same Gaussian filter used to blur the simulated MCAT attenuation map.

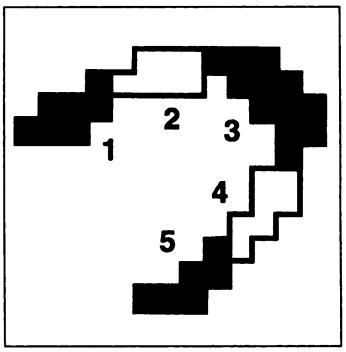

FIGURE 3. Graphical depiction of the five ROIs in the left ventricle wall for which the average, normalized s.d. of pixel values was calculated.

Data Reconstruction

All data were reconstructed with nonuniform attenuation compensation only, using the ML-EM algorithm with stopping points of 25, 50 and 75 iterations. The choice of 25, 50 and 75 iterations for stopping points was somewhat arbitrary. For the unfiltered, noise-free images, the reconstruction was carried up to 75 iterations. Beyond 75 iterations, the unfiltered images did not change appreciably except for a small increase in image noise, which was due to the small amount of statistical noise present in the "noise-free" emission projection data, as noted in the previous section. For the unfiltered noisy images, the reconstruction was carried up to only 50 iterations, because by 50 iterations the statistical noise masked any further changes in the underlying count density. Typically, clinical cardiac studies use heavily filtered images. For such heavily filtered images, stopping points of 25–30 iterations are typically used, because the higher iterations primarily contribute high-frequency information (*17*) which is suppressed by the filter. Therefore, this study also will show results using a 25-iteration stopping point so that the results may be more clinically relevant.

All images were reconstructed into 64 × 64 slices with a pixel width and slice thickness of 0.625 cm. The analysis was performed for both unfiltered images (no postreconstruction filtering) and images filtered using a Butterworth filter of order 5 and cutoff 0.22 cycles/pixel (0.352 cycles/cm).

The Noise Measure: Normalized Standard Deviation

In the noisy reconstructed images, the noise level was measured by calculating the average normalized s.d. of the pixels in specified ROIs within the LV wall. First, the normalized s.d. (NSD) of each pixel in the ROI was calculated by dividing the pixel s.d. by the pixel mean value as follows:

$$\mathrm{NSD}_i = \frac{\text{Estimated s.d. at pixel i}}{\text{Ensemble mean value at pixel i}} = \frac{\left[\frac{1}{N-1}\sum_{n=1}^{N}(x_{i,n}-\mu_i)^2\right]^{1/2}}{\mu_i}, \quad \text{Eq. 1}$$

where $x_{i,n}$ is the value at pixel i for noise realization n, μ_i is the ensemble mean value of pixel i and N is the number of noise realizations. Second, the NSD was averaged over all pixels in the ROI to obtain the average NSD. For this study we calculated the pixel mean and the pixel s.d. using 400 realizations (N = 400) of noisy data.

The ROIs were created by dividing the LV wall, for one transaxial slice, into five regions as shown in Figure 3. In these regions the pixel mean value was approximately constant so differences in the NSD mainly reflect differences in the s.d., not the pixel mean value. The single transaxial slice used for all the noise calculations was the slice, modeling normal ^{201}Tl uptake, shown in the top row of Figure 2.

RESULTS

Analysis of Simulated, Noise-Free Images

The results in this section will be presented for different iteration stopping points (25, 50 and 75 iterations) only where notable differences were observed in the reconstructed images. Furthermore, the results in this section are presented for the unfiltered images only. The results for the filtered noise-free images were essentially the same as the results for the unfiltered noise-free images with the following two exceptions: (a) a reduction in the small amount of image noise at 75 iterations and (b) a small, overall loss of resolution and defect contrast in the filtered noise-free images. Any differences between the 180° and 360° images are greater and more apparent in the unfiltered images than in the filtered images.

The images in Figures 2 and 4 show, for two separate transaxial slices through the LV wall, the radionuclide distribution phantom along with the corresponding noise-free reconstructed images at 25 and 75 iterations. For both Figures 2 and 4, the images in the top row show normal (no myocardial defects) ^{201}Tl uptake, while the images in the bottom row show ^{201}Tl uptake with the simulated perfusion defect.

The reconstructed images in Figure 2 show that toward the right-posterior region of the patient, there are small but noticeable differences between the 180° and 360° images, as indicated by the dotted-line arrows. In particular, the edges of the liver and the very basal edges of the LV wall appear to be less sharp in the 180° images as compared to the 360° images. For the images of Figure 4, the differences between the 180° and 360°

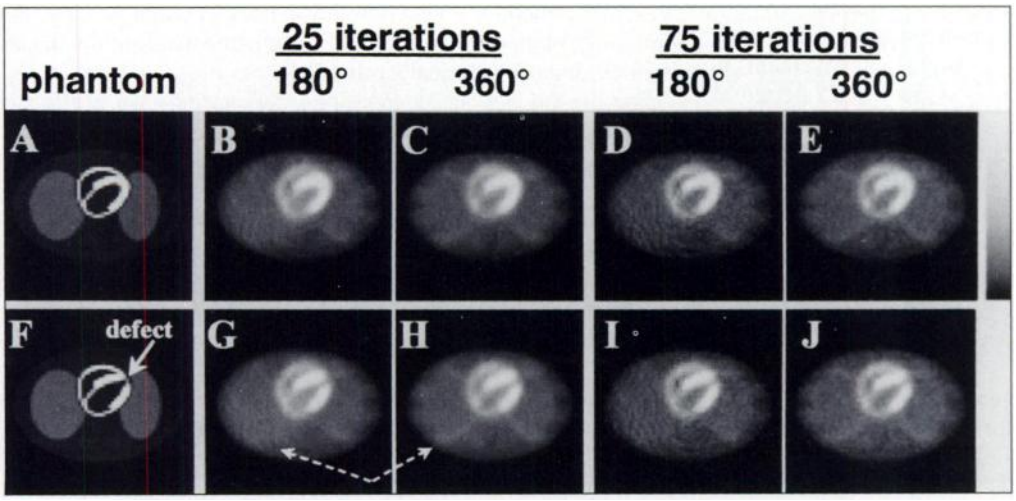

FIGURE 4. (B,D) Images reconstructed from 180° and (C,E) 360° noise-free data along with (A) the corresponding MCAT phantom slice modeling normal ^{201}Tl uptake in the myocardium. For the same slice as A–E, images reconstructed from (G,I) 180° and (H,J) 360° noise-free data along with (F) the corresponding MCAT phantom slice modeling a cold defect in the anterior LV wall.

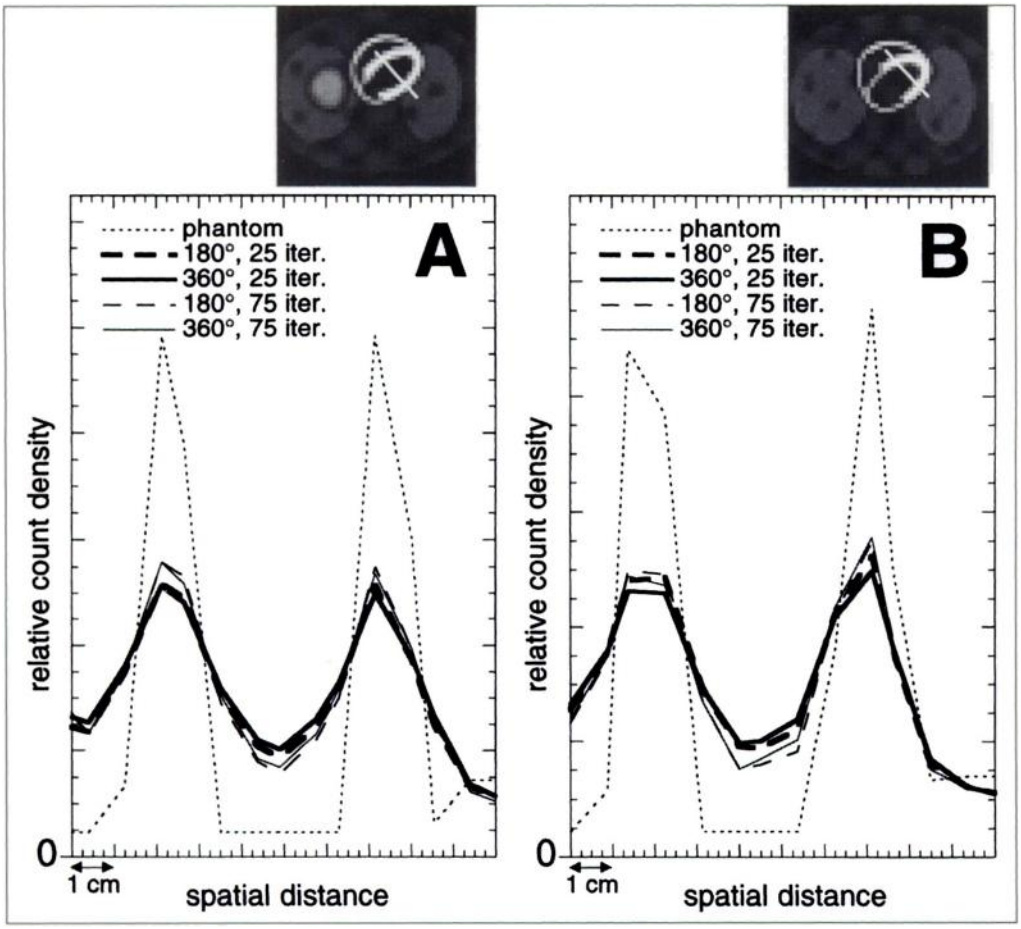

FIGURE 5. Profiles through both walls of the LV of (A) the images shown in the top row of Figure 2 and (B) the images shown in the top row of Figure 4. Profiles show that for normal radionuclide uptake, the spatial resolution and contrast of the left ventricle walls with respect to the background are nearly identical for images reconstructed from 180° and 360° data. The profiles also show a slight increase in contrast for 75 iterations as compared to 25 iterations. Images were normalized to the same average count density before taking the profiles.

images in the right-posterior region of the patient are not apparent, although the edges of the right lung are slightly sharper in the 360° images, as indicated by the dotted-line arrows. These small differences are due, in part, to the depth-dependent collimator response effect which was not compensated for in the reconstruction and, in part, to differences in how the 180° and 360° images converge.

The region of clinical interest, however, is the region within and immediately around the LV wall. In this region, the 180° and 360° images appear to be nearly identical in terms of the overall shape, contrast and spatial resolution of the LV walls. Normalized profiles of the reconstructed images, through both the septal and lateral walls of the LV, are shown in Figures 5A and B, for the images in Figures 2 and 4, respectively. The profiles show that the contrast (relative to the LV chamber) and spatial resolution of the LV walls are nearly equal for the 180° and 360° images, with the 180° images showing slightly higher contrast. The profiles also show a slight improvement in contrast if the iterative reconstruction is stopped at 75 iterations as compared to 25 iterations.

The defect contrast was visually compared by taking profiles across each defect. The profiles are shown in Figures 6A and B for the anterior and basal defects, respectively. In addition, the defect contrast with respect to the LV wall was explicitly calculated from the transaxial slices as:

$$\text{Defect contrast} = \frac{\text{Average CD}_{\text{normal}} - \text{Average CD}_{\text{defect}}}{\text{Average CD}_{\text{normal}}}. \quad \text{Eq. 2}$$

The "average CD_{defect}" is the average count density in a five-pixel ROI placed at the center of the defect. The "average CD_{normal}" is the average count density in a 10-pixel ROI which is the union of two separate five-pixel ROIs placed in regions of apparently normal count density on either side of the defect. Table 1 lists the calculated defect contrast values at 25 and 75 iterations.

Both the profiles and the calculated contrast values yield the same results. Defect contrast is similar in both the 180° and 360° images, for both defect locations, with the anterior defect showing slightly higher (better) contrast in the 180° image and the basal defect showing slightly higher contrast in the 360° image. Defect contrast in all cases is consistently, but only slightly, higher at 75 iterations as compared to 25 iterations.

As stated previously, of clinical interest is the relative distribution of count density in the LV wall itself. To analyze the relative differences in count density in the entire LV wall, bull's-eye plots were constructed from the 180° and 360° reconstructed images. Because this study is primarily concerned with relative and not absolute differences in count density, the bull's-eye plots were normalized to the same maximum value as is often done for clinical evaluations.

For the images at 25 iterations, the normalized bull's-eye plots for both normal and defective myocardial uptake are shown in Figure 7, and the corresponding average values of those bull's-eye plots, within the nine ROIs shown in Figure 8, are listed in the first three columns of Tables 2, 3 and 4 for the cases of normal uptake, anterior defect present and lateral defect present, respectively. For each, the bull's-eye plots of the phantom LV count density (Fig. 7A, D, G) are provided for reference. The bull's-eye plots of the reconstructed images at 50 and 75 iterations look essentially the same as those at 25 iterations and are not shown here. In both the presence and absence of a myocardial defect, the 180° and 360° bull's-eye plots visually show roughly the same distribution of count density with some small differences.

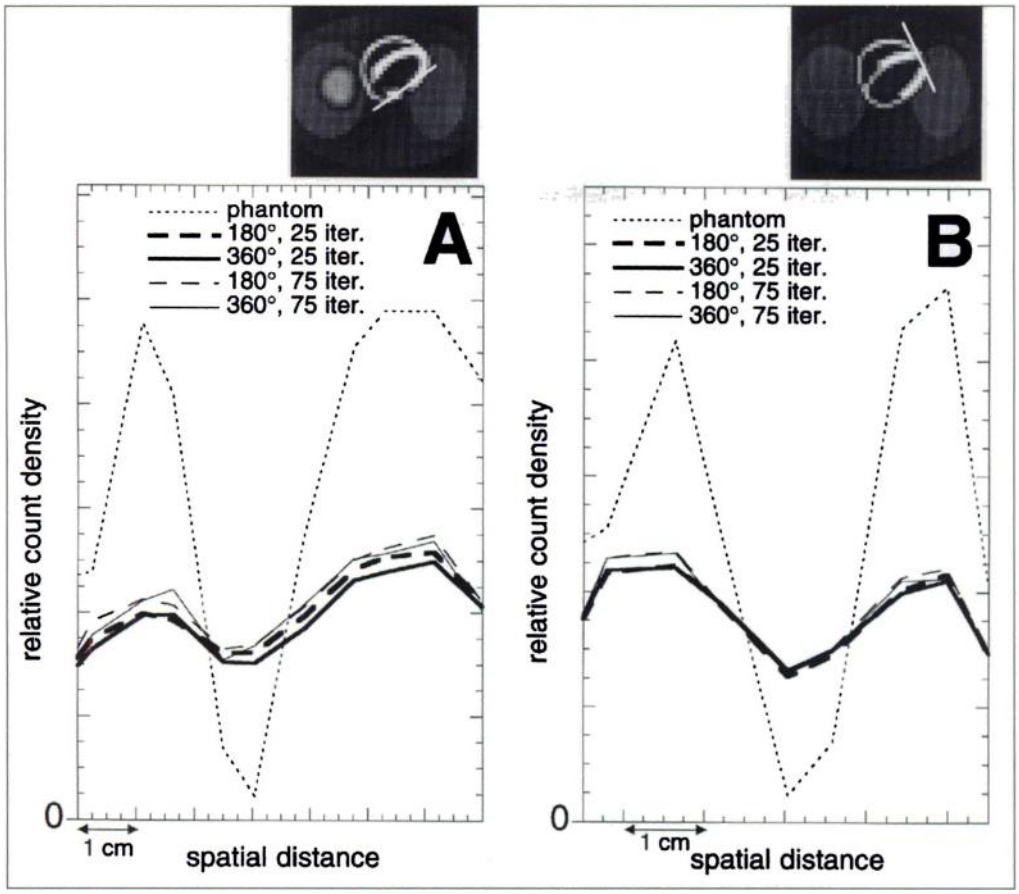

FIGURE 6. Profiles through the simulated (A) basal and (B) anterior myocardial defects of the images shown in the bottom row of Figures 2 and 4. The profiles in A show that basal defect contrast is slightly lower for the 180° images as compared to the 360° images. The profiles in B show that anterior defect contrast is nearly identical but slightly higher for the 180° images as compared to the 360° images. Images were normalized to the same average count density before taking the profiles.

The bull's-eye plots show some artifactual inhomogeneity due to factors, such as collimator-detector response and scatter effects, which have not been compensated for. There is also some inhomogeneity due to "partial volume effect" which results in a lower count density in pixels that are not comprised entirely of myocardium. The partial volume effect explains the inhomogeneity seen in the phantom bull's-eye plots of Figure 7. Since these artifactual inhomogeneities in count density are common to both the 180° and 360° images, it is clear that they are not a function of whether 180° or 360° acquisition was used.

To directly compare the relative differences in count density between the 180° and 360° images, for each point in the bull's-eye plot, the relative difference in count density was calculated as:

$$\text{Relative difference}_{180°,\,360°} = \frac{180° \text{ bull's-eye} - 360° \text{ bull's-eye}}{360° \text{ bull's-eye}}. \quad \text{Eq. 3}$$

TABLE 1
Defect Contrast Measured from a Single, Transaxial Slice

Defect location	Acquisition	Defect contrast* 25 iterations	Defect contrast* 75 iterations
Anterior	180°	0.45	0.46
	360°	0.43	0.46
Basal-lateral	180°	0.26	0.29
	360°	0.29	0.31

*True defect contrast for anterior defect = 0.84; true defect contrast for basal-lateral defect = 0.87.

The resulting relative difference plots, calculated from the count densities at 25, 50 and 75 iterations are shown in Figure 9. The relative difference plots change noticeably from 25–75 iterations (beyond 75 iterations the relative difference plot did not change appreciably) because the 180° and 360° images have not yet completely converged at 25 and 50 iterations. At 25 iterations the 180° images show higher count density than the 360° images in large, contiguous areas in the septal and lateral walls, but by 75 iterations this pattern has changed and the relative differences between the 180° and 360° images are smaller.

Although the changes in the relative differences between 25 and 75 iterations look dramatic on the plots in Figure 9, the relative difference in count density, for all three iteration stopping points, is less than 4.5% over most of the LV wall and is never greater than 5.2% at any point in the bull's-eye plot. The rightmost column in Tables 2, 3 and 4, for the cases of normal uptake, anterior defect present and lateral defect present, respectively, lists the corresponding average values of the relative difference plot at 25 iterations for the nine ROIs. The average relative difference between the 180° and 360° images is never greater than 4% in any of the nine regions of the LV wall. Relative differences at this level are generally not visually apparent in the noise-free images and almost certainly will not be apparent in noisy SPECT images.

Analysis of Experimental, Low-Noise Images

To validate the simulation results, the same analysis used in the previous section was applied to the experimental phantom data. In general, the results were the same for the experimental data as for the simulated data.

As in the previous section, the results in this section will be presented for different iteration stopping points (25, 50 and 75

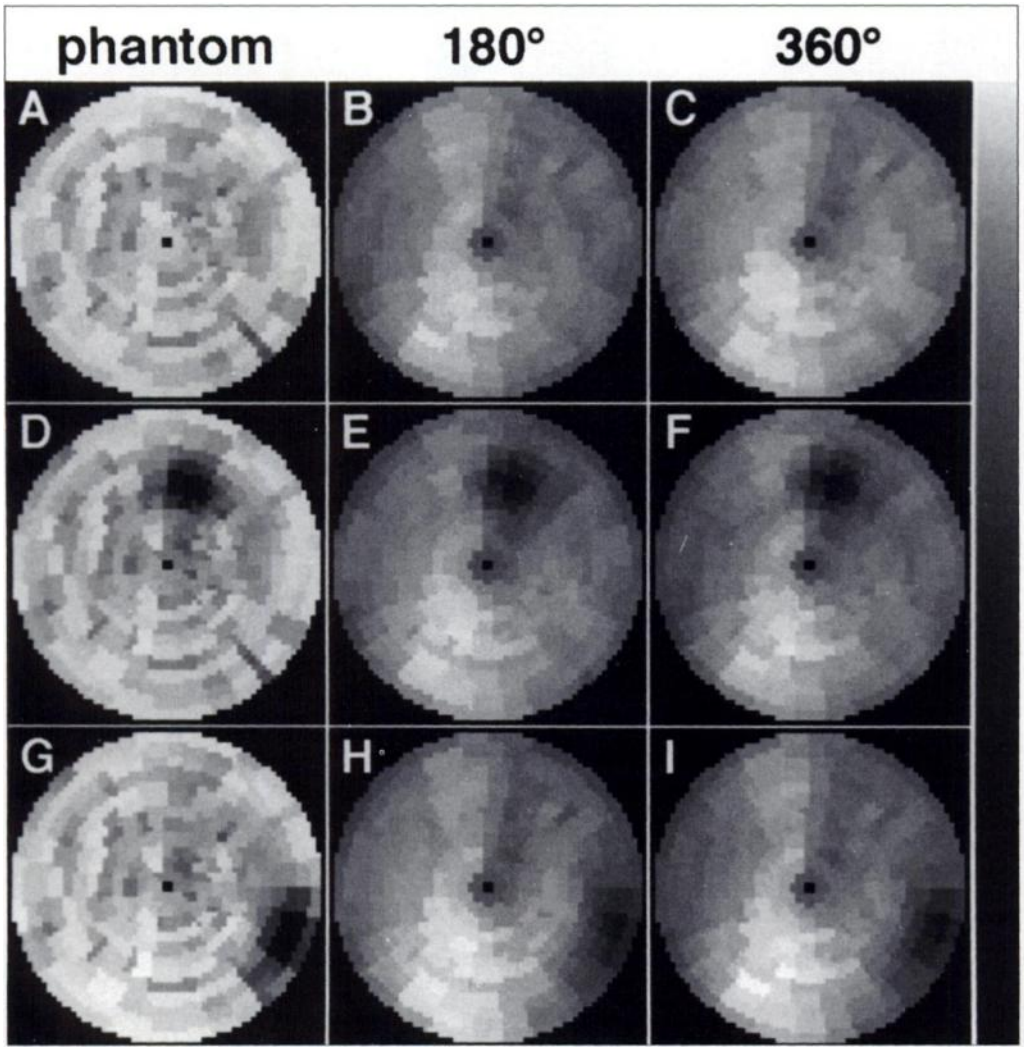

FIGURE 7. Bull's-eye plots showing the distribution of count density in the LV wall of the phantom and the reconstructed images at 25 iterations for normal radionuclide uptake (A–C), for uptake in the presence of the anterior defect (D–F) and for uptake in the presence of a basal defect (G–I). The bull's-eye plots have been individually normalized to a maximum value of 100. The bull's-eye plots of the reconstructed images at 50 and 75 iterations look essentially the same as those shown here.

iterations) only where notable differences were observed in the reconstructed images. Unless otherwise noted, the results in this section are presented for the unfiltered images only. As for the simulated data, the results for the filtered noise-free images were essentially the same as the results for the unfiltered noise-free images with the following two exceptions: (a) a reduction in the small amount of image noise at 75 iterations and (b) a small, overall loss of resolution.

Figure 10 shows, for two separate transaxial slices through the LV wall, the reconstructed images of the experimental phantom data at 25 and 75 iterations. The slice shown in Figures 10A through D is superior to the slice shown in Figures 10E through H by 3.0 cm (5 slices). In the right-posterior region of the phantom, there are small but noticeable differences between the 180° and 360° images, as indicated by the dotted-line arrows. In particular, the edge of the spine (which has no activity) is visible in the 360° images but not in the 180° images, and, in the bottom row of images, the edge of the liver appears to be less sharp in the 180° images as compared to the 360° images. Also, at 75 iterations, there is a noticeable difference in the noise texture between the 180° and 360° images in the right-posterior region.

In the myocardial region, the 180° and 360° images appear to

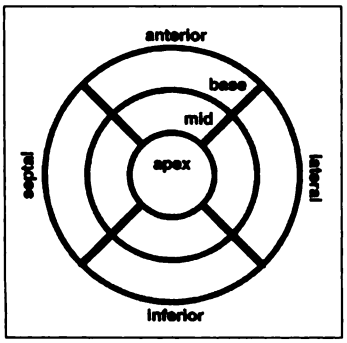

FIGURE 8. Graphical depiction of the nine bull's-eye-plot ROIs used to calculate the average values in Tables 2, 3 and 4.

TABLE 2
Regional Count Densities and Relative Differences in the LV Wall with Normal Uptake (25 iterations)

		Average normalized* count density in ROI			Average relative difference in ROI (%)		
					180°-phan	360°-phan	180°-360°
ROI		Phantom	180°	360°	phan	phan	360°
Apex		93	86	85	−7	−8	+1
Mid	Septal	93	90	86	−3	−7	+4
	Anterior	91	86	86	−5	−6	<1
	Lateral	91	87	84	−3	−7	+4
	Inferior	93	94	93	+1	0	+1
Base	Septal	93	84	80	−10	−13	+4
	Anterior	93	84	84	−10	−10	<1
	Lateral	95	84	82	−11	−14	+3
	Inferior	94	93	90	−2	−4	+2

* Bull's-eye plots were individually normalized to a maximum value of 100.0.

TABLE 3
Regional Count Densities and Relative Differences in the LV Wall with Anterior Defect (25 iterations)

ROI		Average normalized* count density in ROI			Average relative difference in ROI (%)		
		Phantom	180°	360°	180°-phan phan	360°-phan phan	180°-360° 360°
Apex		89	84	84	−5	−5	<1
Mid	Septal	93	89	86	−4	−7	+3
	Anterior†	72	73	73	+8	+9	−1
	Lateral	90	85	83	−5	−8	+3
	Inferior	93	93	93	<1	<1	<1
Base	Septal	93	83	81	−11	−13	+3
	Anterior	93	81	82	−13	−12	−1
	Lateral	95	83	82	−12	−14	+2
	Inferior	94	92	90	−3	−4	+1

* Bull's-eye plots were individually normalized to a maximum value of 100.0.

† ROI containing the defect: in this ROI the count density in the phantom ranges from high (>90) to very low (~30), while the count density in the reconstructed images ranges from moderately high (~85) to moderately low (~50). Therefore, the average relative difference between the reconstructed images and the phantom is high in this region (+8, +9) despite the similar average count density values.

be nearly identical in terms of the overall shape, contrast and spatial resolution of the LV walls. Normalized profiles through both the septal and lateral walls of the LV of Figures 10A through D are shown in Figure 11A, while normalized profiles through both the posterior and anterior walls of the LV of Figures 10E through F are shown in Figure 11B. The profiles show that the contrast (relative to the LV chamber) and spatial resolution of the LV walls are nearly equal for the 180° and 360° images. The profiles also show a slight improvement in contrast if the iterative reconstruction is stopped at 75 iterations as compared to 25 iterations.

For the images at 25 iterations, the normalized bull's-eye plots for both normal and defective myocardial uptake are shown in Figure 12. The bull's-eye plots of the reconstructed images at 50 and 75 iterations look essentially the same as those at 25 iterations and are not shown here. The 180° and 360° bull's-eye plots visually show roughly the same distribution of count density with some small differences.

Both the transaxial slices and bull's-eye plots show an artifactual increase in count density in the inferior wall of the LV near the apex. This is largely due to scatter from the liver-stomach compartment which is situated very close to the inferior LV wall near the apex. Since both the 180° and 360° images show the same artifactual increase in count density, it is clear that it is not a function of whether a 180° or a 360° acquisition was used.

The relative difference plots were calculated using Equation 3 for the unfiltered images. Because the experimental data are low-noise instead of noise-free, by 75 iterations statistical noise becomes great enough that the bull's-eye plot analysis did not yield meaningful results about systematic differences between the 180° and 360° images. For *unfiltered* images at 25 iterations, the relative differences (due to both noise and any systematic differences) between the 180° and 360° bull's-eye plots were in the range −5.2% to 6.3%, while at 75 iterations the relative differences were in the range −7.1% to 7.8%.

The relative difference plots were calculated using *filtered* images and are shown in Figure 13, for 25, 50 and 75 iterations. For the filtered images, the relative difference in count density, for all three iteration stopping points, is less than 4.5% over most of the LV wall and is never greater than 7.3% at any point in the bull's-eye plot. The first and second columns in Table 5 list the corresponding average values of the relative difference plot at 25 iterations for the nine ROIs. The third column in Table 5 lists the average relative difference which is never greater than 3% in any of the nine regions of the LV wall.

TABLE 4
Regional Count Densities and Relative Differences in the LV Wall with Basal/Lateral Defect (25 iterations)

ROI		Average normalized* count density in ROI			Average relative difference in ROI (%)		
		Phantom	180°	360°	180°-phan phan	360°-phan phan	180°-360° 360°
Apex		89	85	85	−5	−5	<1
Mid	Septal	93	90	86	−3	−7	+4
	Anterior	91	85	85	−6	−6	<1
	Lateral	89	85	82	−5	−8	+3
	Inferior	93	94	93	+1	<1	+1
Base	Septal	93	84	80	−10	−14	+4
	Anterior	93	84	84	−10	−10	<1
	Lateral†	73	71	69	+9	+5	+4
	Inferior	94	90	88	−4	−6	+2

* Bull's-eye plots were individually normalized to a maximum value of 100.0.

† ROI containing the defect: in this ROI the count density in the phantom ranges from high (>90) to very low (~30), while the count density in the 180° image ranges from moderately high (~85) to moderately low (~50). Therefore, the average relative difference between the 180° image and the phantom is high in this region (+9) despite the similar average count density values.

Analysis of Noise Level for Multidetector Systems

In the previous two sections, we demonstrated that in the LV region the noise-free 180° and 360° images are nearly identical with respect to contrast, resolution and artifacts. In this section, 180° and 360° images are compared with respect to the relative noise levels in the LV wall. The relative noise level is dependent on the detector system geometry. Two popular multidetector geometries were compared in this study.

First, the noise level in the 180° and 360° images was compared for a dual-detector system with the detectors oriented at 90° to each other. For this system geometry, 180° data are acquired with a 90° detector rotation and 360° data are acquired with a 360° detector rotation[1], as shown in Figure 14A. Assuming the same total scan time for 180° and 360° data acquisition, each *detector* spends 1/4 of the time per view acquiring the 360° data as compared to the 180° data. However, each view is sampled twice, once by each detector, so effectively 1/2 of the time per view is spent acquiring the 360° data as compared to the 180° data ($T_{dual,360°} = T_{dual,180°}/2$, where T is the time per view).

Assuming 1/2 of the time per view for the 360° data, as compared to the 180° data, the noise-free data were scaled and noise was simulated as described previously. For the five ROIs,

[1]For this detector geometry, the minimum detector rotation required for the acquisition of 360° data is 270°. However, for a detector rotation of 270°, the acquisition time per view is not equal for all views because half of the views are acquired twice (once by each detector), and half are only acquired once. For the same total scan time and equal acquisition time per view within a scan, a full 360° rotation with each view sampled twice yields more acquired LV counts and better image statistics than a 270° rotation with each view sampled once. Therefore, a 360° detector rotation is optimal for the collection of 360° data.

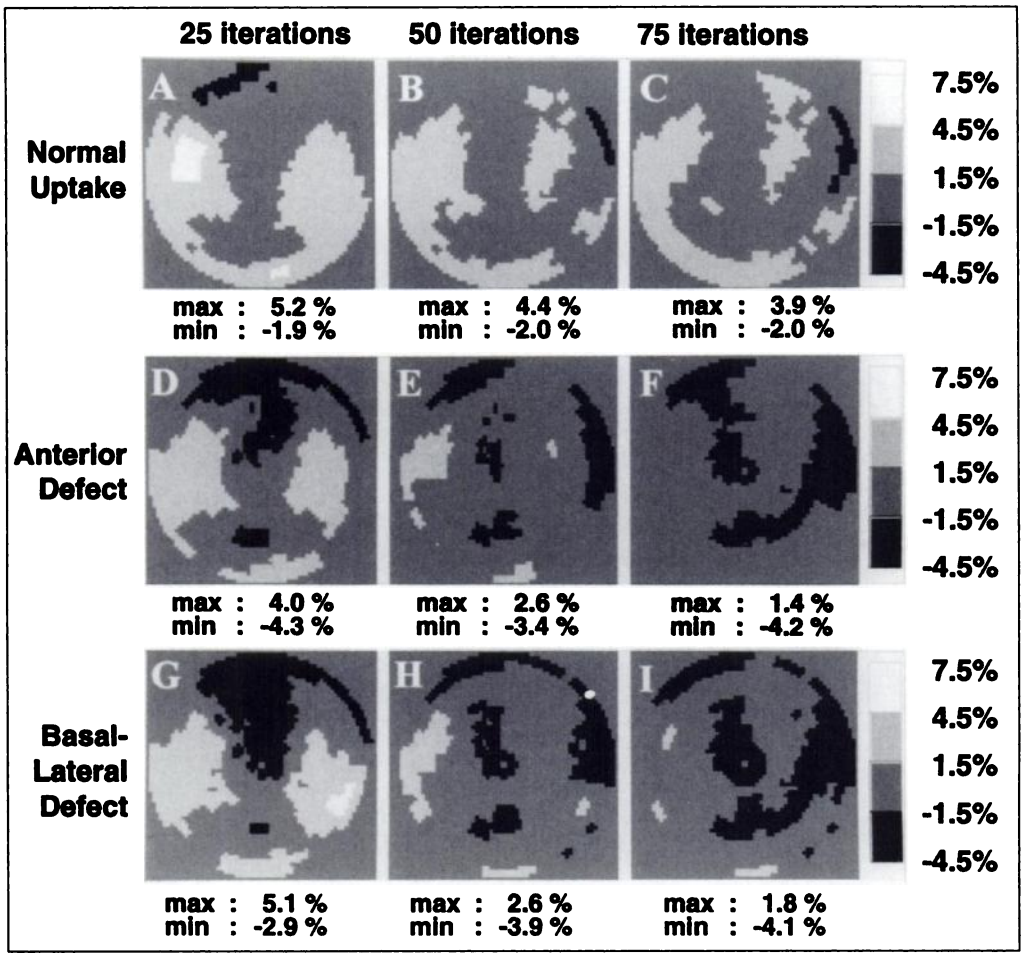

FIGURE 9. Plots showing the relative difference between the 180° and 360° bull's-eye plots at 25, 50 and 75 iterations. The relative difference, calculated using Equation 3, is plotted for (A–C) normal radionuclide uptake, for (D–F) uptake in the presence of the anterior defect and (G–I) for uptake in the presence of the basal defect. Under each plot is listed the maximum and minimum values for that plot.

the average NSDs for unfiltered and filtered images are plotted in Figures 15A and 16A, respectively, for both 25 and 50 iterations of ML-EM. As expected, the noise increases with increasing depth from the edge of the torso and with increasing iteration number. For all five ROIs, the 180° images have a lower average NSD than the 360° images. Therefore, with respect to noise level in the LV wall, 180° data acquisition is superior to 360° data acquisition for the 90° dual-detector system. These results also would apply to a single-detector system.

Second, the noise level in 180° and 360° images was compared for a triple-detector system with the detectors oriented at 120° to each other. For this system geometry, both 180° data and 360° data are acquired with a 120° detector rotation, as shown in Figure 14B. The 180° data are obtained by simply discarding half of the 360° data. Assuming the same total scan time for 180° and 360° data acquisition, the same time per view is spent acquiring the 360° data as compared to the 180° data ($T_{triple,360°} = T_{triple,180°}$).

Assuming the same time per view for the 360° data as

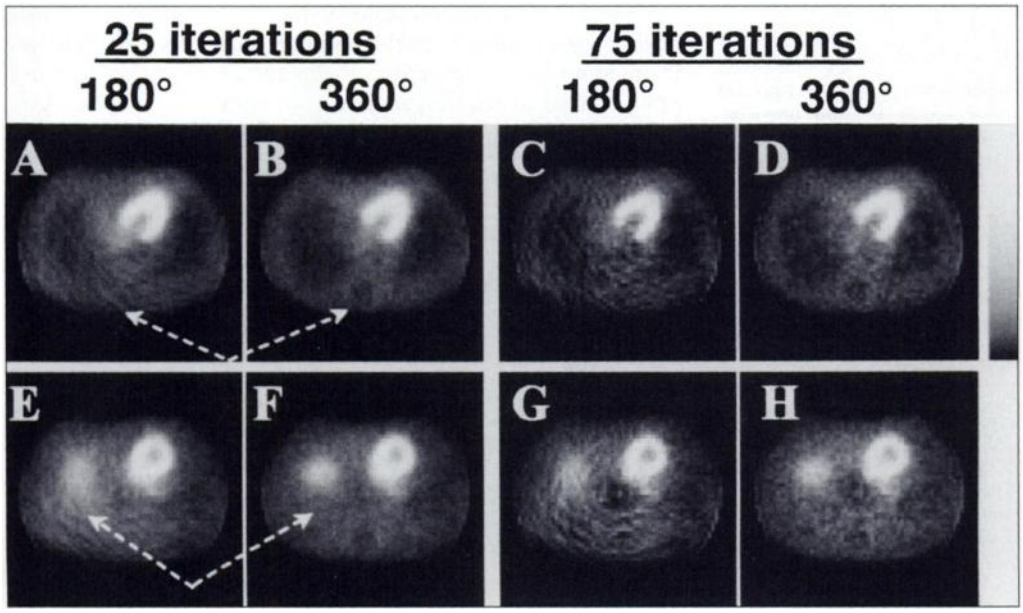

FIGURE 10. Images reconstructed from 180° and 360° low-noise experimental phantom data modeling normal ^{201}Tl uptake in the myocardium. The transaxial slice shown in images A–D is 3.0 cm superior to the slice shown in images E–H.

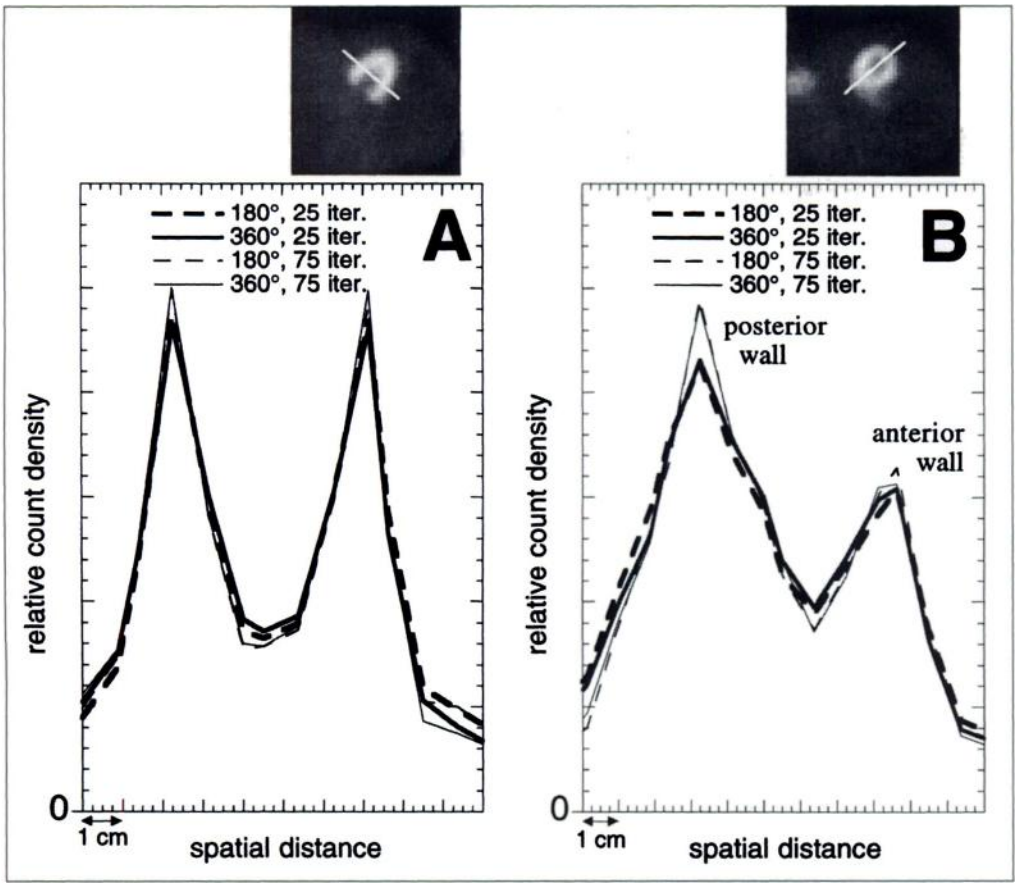

FIGURE 11. Plot A shows profiles through the septal and lateral walls of the LV of the images shown in the top row of Figure 10 while Plot B shows profiles through the posterior-inferior and anterior walls of the LV of the images shown in the bottom row of Figure 10. Profiles show that the spatial resolution and contrast of the left ventricle walls, with respect to the background, is nearly identical for images reconstructed from 180° and 360° data. The profiles also show a slightly improved resolution and contrast for 75 iterations as compared to 25 iterations. Images were normalized to the same average count density before taking the profiles.

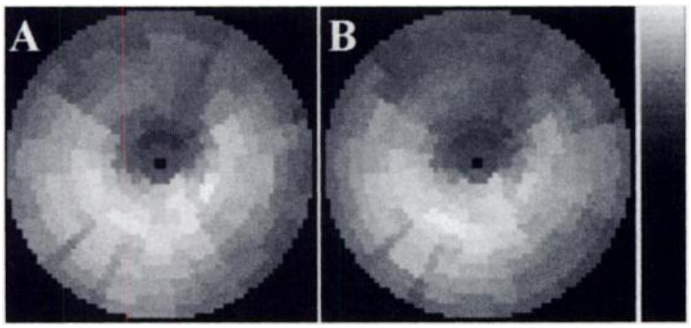

FIGURE 12. Bull's-eye plots showing the distribution of count density in the LV wall of the images reconstructed from experimental phantom data at 25 iterations for (A) 180° and (B) 360° data. The bull's-eye plots have been individually normalized to a maximum value of 100. The bull's-eye plots of the reconstructed images at 50 and 75 iterations look essentially the same as those shown here, except for some increase in statistical noise. The increase in count density in the basal-inferior region, seen in both the 180° and 360° images, is due to scatter from the liver-stomach compartment.

compared to the 180° data, the noise-free data were scaled and noise was simulated as described previously. For the five ROIs, the average NSDs for unfiltered and filtered images are plotted in Figures 15B and 16B, respectively, for both 25 and 50 iterations of ML-EM. Once again, the noise increases with increasing depth from the edge of the torso and with increasing iteration number. For all five ROIs, the 180° images have higher average NSDs than the 360° images. Therefore, with respect to noise level in the LV wall, 360° data acquisition is superior to 180° data acquisition for the 120° triple-detector system.

With respect to noise level in the LV wall, it has just been shown that 180° data acquisition is superior to 360° data acquisition for the 90° dual-detector system and that 360° data acquisition is superior to 180° data acquisition for the 120° triple-detector SPECT system. In this third and final comparison, the noise level in images reconstructed from 180° data

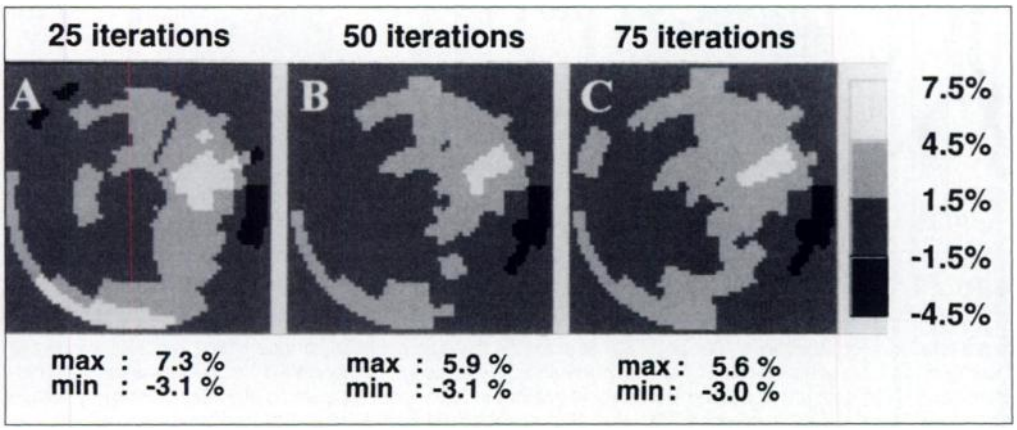

FIGURE 13. Plots showing the relative difference between the 180° and 360° bull's-eye plots at (A) 25, (B) 50 and (C) 75 iterations, for the experimental phantom data. The relative difference was calculated from *filtered* images using Equation 3. The maximum and minimum values are listed beneath each plot.

TABLE 5
Regional Count Densities and Relative Differences in the LV Wall for Experimental Data with Normal Uptake (25 iterations)

ROI		Average normalized* count density in ROI 180°	Average normalized* count density in ROI 360°	Average relative difference in ROI % 180°-360° / 360°
Apex		77	79	−3
Mid	Septal	86	88	−2
	Anterior	77	76	−1
	Lateral	88	85	+3
	Inferior	93	92	+1
Base	Septal	79	78	+1
	Anterior	73	73	0
	Lateral	76	76	0
	Inferior	80	78	+2

* Bull's-eye plots were individually normalized to a maximum value of 100.0.

acquired with the 90° dual-detector system was compared to that of images reconstructed from 360° data acquired with the 120° triple-detector system. For this comparison, the 180° data are acquired with a 90° detector rotation and the 360° data are acquired with a 120° detector rotation, as shown in Figure 14C. Assuming the same total scan time for 180° and 360° data acquisition, 3/4 of the time per view is spent acquiring the 360° data using the triple-detector system as compared to the 180° data using the dual-detector system ($T_{triple,360°} = 3T_{dual,180°}/4$).

Assuming 3/4 of the time per view for the 360° data as compared to the 180° data, the noise-free data were scaled and noise was simulated as described previously. For the five ROIs, the average NSDs for unfiltered and filtered images are plotted in Figures 15C and 16C, respectively, for both 25 and 50 iterations of ML-EM. The average NSD is nearly equal in all the ROIs for the 180° and 360° images, with the average NSD slightly lower for the 180° images in the apical region of the LV wall and slightly greater in the basal region of the LV wall.

DISCUSSION

For a medium-large patient, a quantitative comparison of the count density distribution in the LV wall in 180° and 360° ^{201}Tl SPECT images showed the difference in count density to be no greater than 6% (of the count density in the 360° image) at any point in the LV wall and to be less than 4.5% over most of the LV wall. These simulation results were validated with experimental phantom data. A quantitative comparison of defect contrast found the differences in defect contrast to be no greater than 3% of the count density in normal areas of LV wall. By comparison, in unfiltered images at typical noise levels for ^{201}Tl SPECT images, the s.d. of count density in the normal LV wall, due to statistical noise, was measured to be between 13% (apex) and 20% (base) of the noise-free count density for 25 iterations of ML-EM and between 19% (apex) and 30% (base) for 50 iterations of ML-EM. Therefore, since the systematic differences in count density between the 180° and 360° images are small, in comparison to the variations in count density due to statistical noise, the systematic differences will not be apparent in the noisy, unfiltered 180° and 360° images.

If a postreconstruction smoothing filter is applied to the images, the results of the quantitative comparison of LV count density and of defect contrast are roughly the same. However, the s.d. of count density due to statistical noise is reduced to between 5% (apex) and 10% (base) of the normal count density for 25 iterations and to between 6% (apex) and 11% (base) for 50 iterations. Since the systematic differences in count density and defect contrast between the 180° and 360° images are approximately equal to or less than differences in count density due to statistical noise, the systematic differences are not likely to be apparent in the noisy, filtered 180° and 360° images.

Defect contrast, in the noise-free images, was slightly better in the 180° images (as compared to the 360° images) for an apical-anterior defect and slightly worse in the 180° images for a basal-lateral defect. However, as just stated, the differences in contrast were small in comparison to variation due to statistical noise and, therefore, the differences in contrast are not likely to be apparent in noisy images.

For the 90° dual-detector system, the noise level was consistently less in the 180° image, and for a 120° triple-detector system the noise level was consistently less in the 360° image. Whether or not the differences in noise level will result in differences in defect detection and diagnosis is questionable, especially since the differences in noise level were extremely small after a smoothing filter (typical of those applied to clinical

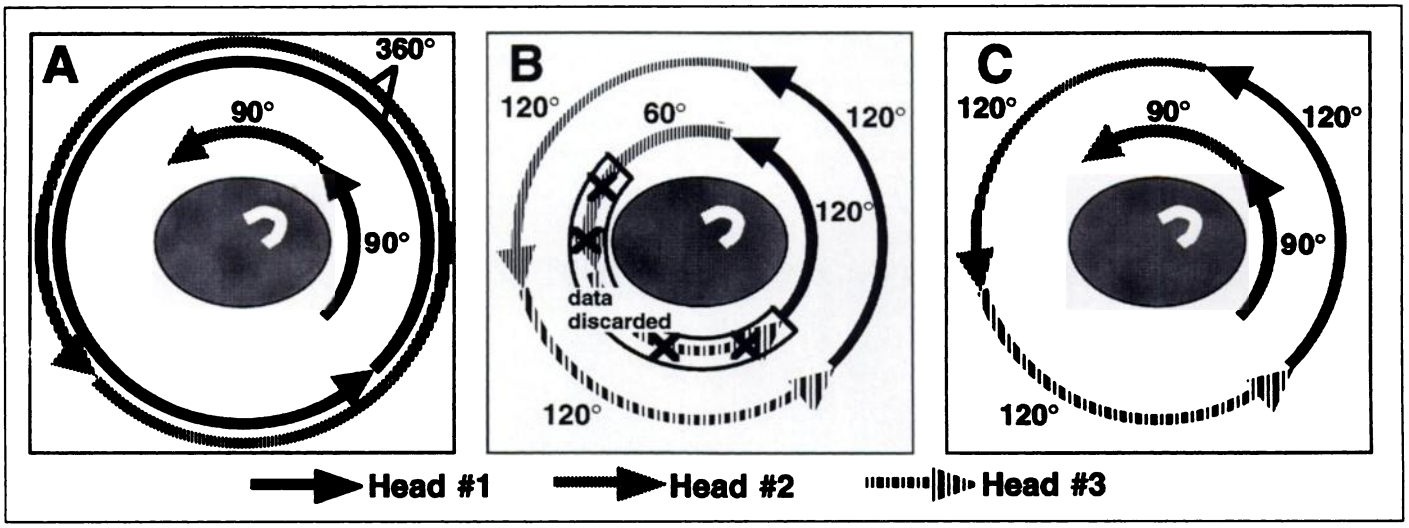

FIGURE 14. Graphical depiction of the detector rotation used to acquire 180° and 360° data for the three comparisons of noisy 180° and 360° images. (A) Using a 90° dual-detector system only, 180° and 360° data are acquired with 90° and 360° rotations, respectively. (B) Using a 120° triple-detector system only, 180° and 360° are both acquired with a 120° rotation (180° data are obtained by discarding half of the 360° data). (C) Using a 90° dual-detector system for the 180° acquisition and a 120° triple-detector system for the 360° acquisition, 180° and 360° are acquired with 90° and 120° rotations, respectively.

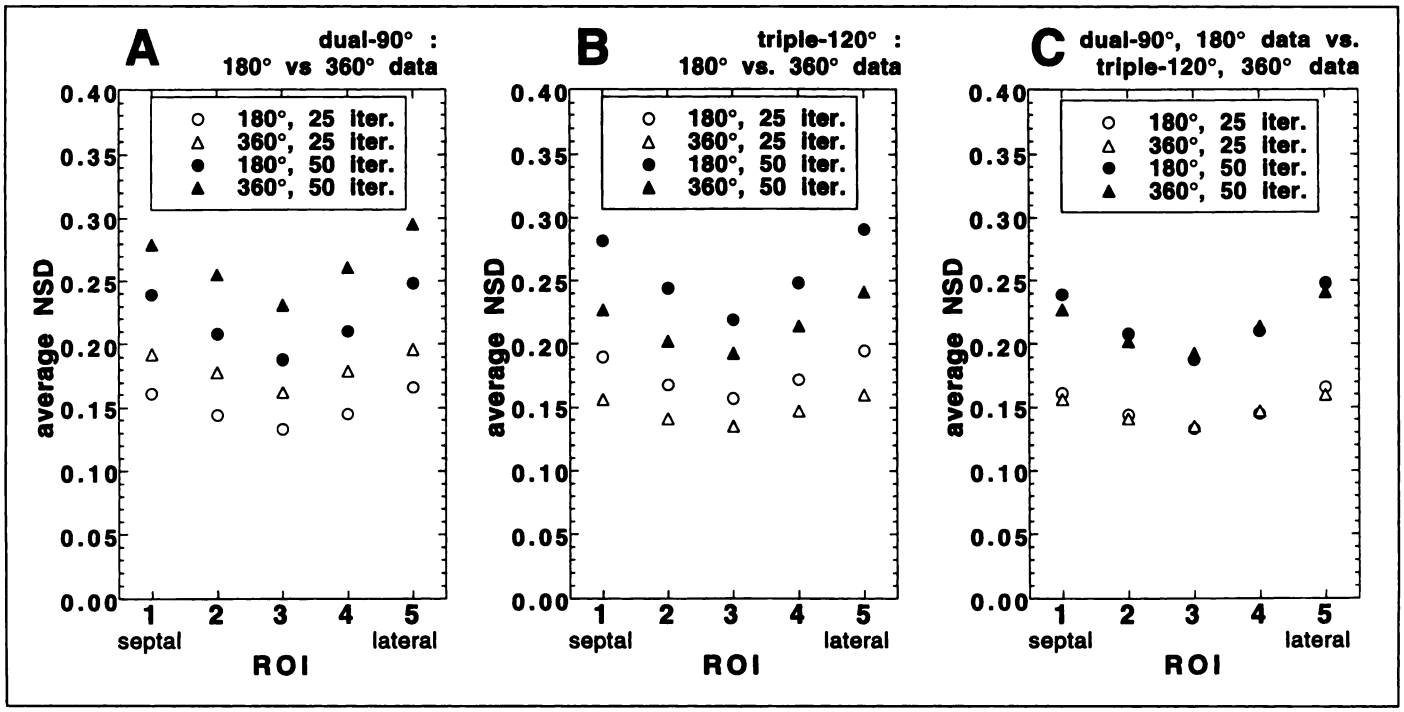

FIGURE 15. The average NSD in *unfiltered*, transaxial images reconstructed from 180° and 360° data acquired on multidetector SPECT systems, in the five ROIs (Fig. 2), for both 25 and 50 iterations of ML-EM. The three comparisons in plots A–C correspond to the multidetector acquisition scenarios shown in Figures 14A–C. Total scan time is the same for all 180° and 360° data acquisitions.

images) was applied to images. For the two multidetector geometries studied, neither geometry appeared to have an advantage over the other in terms of reducing image noise. The acquisition schemes that produced the lowest image noise for each system (i.e., 180° data collection for the 90° dual-detector system and 360° data collection for the 120° triple-detector system), produced roughly the same level of noise in the respective images, even without filtering.

CONCLUSION

This study shows that when attenuation compensation is used in reconstructing ^{201}Tl SPECT images from 180° and 360° data, these images are essentially identical in the myocardial region, even for a medium-large patient. Systematic differences in myocardial count density between the 180° and 360° images were small. For filtered images, differences in the noise level in the myocardium were small as well. This is true when the 45°

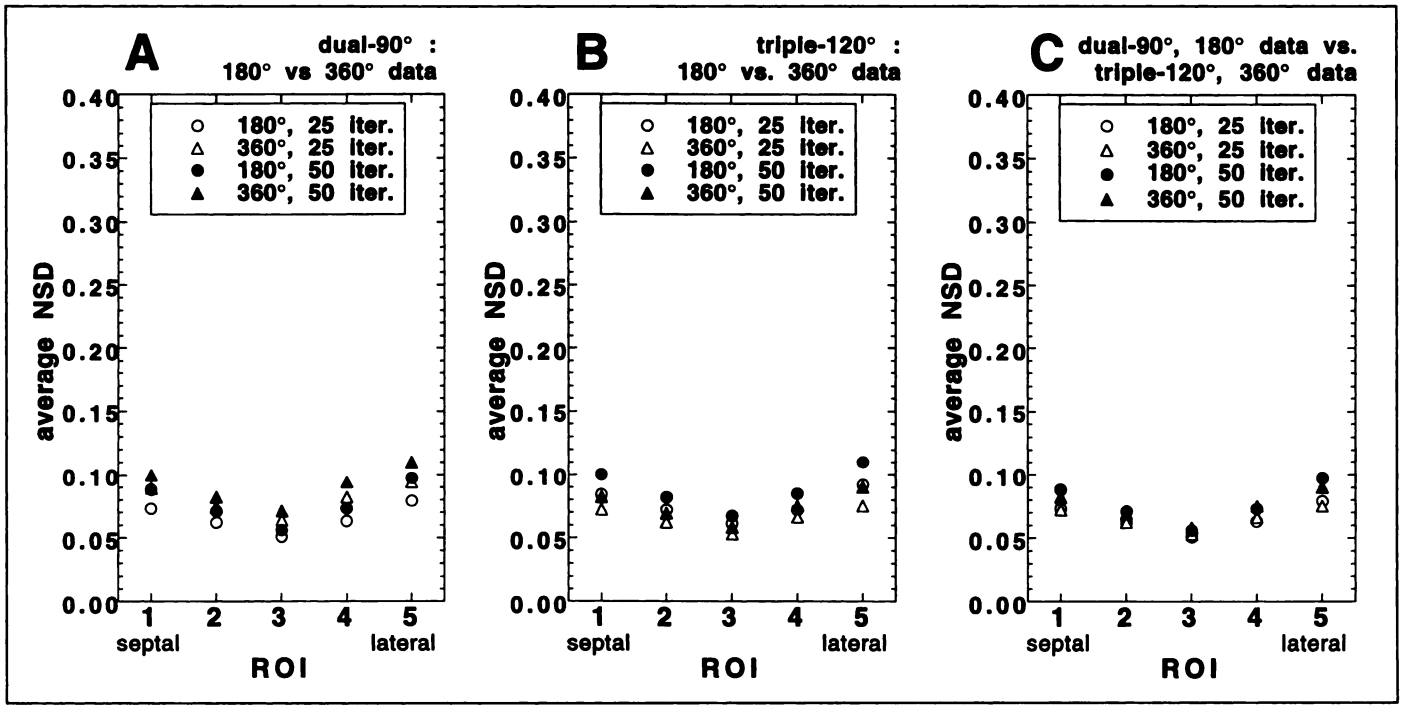

FIGURE 16. The average NSD in *filtered*, transaxial images reconstructed from 180° and 360° data acquired on multidetector SPECT systems, in the five ROIs (Fig. 2), for both 25 and 50 iterations of ML-EM. The three comparisons in plots A–C correspond to the multidetector acquisition scenarios shown in Figures 14A–C. Total scan time is the same for all 180° and 360° data acquisitions.

RAO to 45° LPO arc is used for the 180° acquisition. There are obvious differences between 180° and 360° images in the right-posterior region of the phantom patient. These simulation and experimental phantom results are consistent with those reported from a clinical study which compared filtered 180° and 360° images using ^{99m}Tc-sestamibi and found no significant difference between 180° and 360° images with respect to either the diagnostic accuracy or defect contrast (*18*).

ACKNOWLEDGMENTS

This work was partially supported by the Public Health Grants #CA50539 and #CA39463 and by American Heart Association Grant-in-Aid #93010880. This work also was supported during the tenure of an Established Investigatorship from the American Heart Association for Dr. Hasegawa. The contents of this work are solely the responsibility of its authors and do not necessarily represent the official views of the Public Health Service or the American Heart Association.

REFERENCES

1. Coleman RE, Jaszczak RJ, Cobb FR. Comparison of 180° and 360° data collection in thallium-201 imaging using SPECT. *J Nucl Med* 1982;23:655–660.
2. Eisner RL, Nowak DJ, Pettigrew R, Fajman W. Fundamentals of 180° acquisition and reconstruction in SPECT imaging. *J Nucl Med* 1986;27:1717–1728.
3. Go RT, MacIntyre WJ, Houser TS, et al. Clinical evaluation of 360° and 180° data sampling techniques for transaxial SPECT thallium-201 myocardial perfusion imaging. *J Nucl Med* 1985;26:695–706.
4. Hoffman EJ. 180° compared with 360° sampling in SPECT [Editorial]. *J Nucl Med* 1982;23:745–746.
5. Knesaurek K, King MA, Glick SJ, Penney BC. Investigation of causes of geometric distortion in 180° and 360° angular sampling in SPECT. *J Nucl Med* 1989;30:1666–1675.
6. Tamaki N, Mukai T, Ishii Y, et al. Comparative study of thallium emission myocardial tomography with 180° and 360° data collection. *J Nucl Med* 1982;23:661–666.
7. Nuyts J, Dupont P, Van den Maegdenbergh V, et al. A study of heart-liver artifact in emission tomography. *J Nucl Med* 1995;36:133–139.
8. LaCroix KJ, Tsui BMW, Hasegawa BH. Comparison of 180° and 360° reconstruction with non-uniform attenuation compensation for ^{201}Tl SPECT. *IEEE Trans Nucl Sci* 1995;42:1276–1281.
9. Lange K, Carson R. EM reconstruction algorithms for emission and transmission tomography. *J Comput Assist Tomogr* 1984;8:306–316.
10. Shepp LA, Vardi Y. Maximum likelihood reconstruction for emission tomography. *IEEE Trans Med Imaging* 1985;MI-1:113–122.
11. Tsui BMW, Terry JA, Gullberg GT. Evaluation of cardiac cone-beam single photon emission computed tomography using observer performance experiments and receiver operating characteristic analysis. *Invest Radiol* 1993;28:1101–1112.
12. Bradley-Moore PR, Lebowitz E, Greene MW, Atkins HL, Ansari AN. Thallium-201 for medical use. II: biological behavior. *J Nucl Med* 1975;16:156–160.
13. Harrison R, Vannoy S, Haynor D, et al. Preliminary experience with the photon history generator module of a public-domain simulation system for emission tomography. In: L. Klaisner, ed. *IEEE Nuclear Science Symposium and Medical Imaging Conference*. San Francisco; IEEE: 1993;2:1154–1158.
14. Meikle S, Dahlbom M, Cherry S. Attenuation correction using count-limited transmission data in positron emission tomography. *J Nucl Med* 1993;34:143–150.
15. Tsui BMW, Zhao X, Lalush D, et al. Pitfalls of attenuation compensation and their remedies in cardiac SPECT [Abstract]. *J Nucl Med* 1994;35(suppl):115P.
16. Li J, Tsui BMW, Welch A, Frey EC, Gullberg GT. Energy window optimization in simultaneous technetium-99m TCT and thallium-201 SPECT data acquisition. *IEEE Trans Nucl Sci* 1995;42:1207–1213.
17. Wilson D. Noise and resolution properties of filtered backprojection and ML-EM reconstructed SPECT images [PhD dissertation]. Chapel Hill, NC; The University of North Carolina at Chapel Hill; 1994.
18. Ficaro EP, Pitt SR, Wawrzynski PE, Rose PA, Corbett, JR. Diagnostic accuracy of 180° and 360° reconstructions for uncorrected and attenuation corrected Tc-99m cardiac SPECT [Abstract]. *J Nucl Med* 1996;37(suppl):81P.

Erratum

Due to a printer error, Figures 1A and 2A in the article, "Diagnosis of Recurrent Glioma with SPECT and Iodine-123-α-Methyl Tyrosine" by Kuwert et al. (*J Nucl Med* 1998;39:23–27) were reversed. The images are reprinted correctly below.

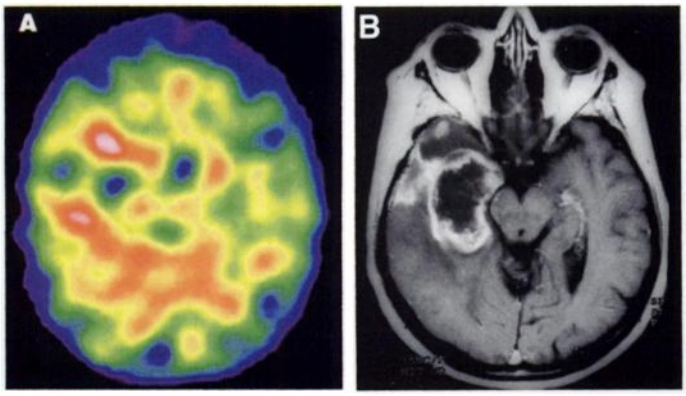

FIGURE 1. Minor IMT uptake in the contrast-enhancing rim of a postsurgical defect (A; transaxial) presented together with the corresponding postgadolinium T1-weighted MRI scan (B) in a patient without clinical deterioration during 13 mo of follow-up after surgery for a glioma IV (Patient 7; IMT uptake ratio = 1.49). The SPECT image is calibrated to its own maximum, with white and red indicating the highest values.

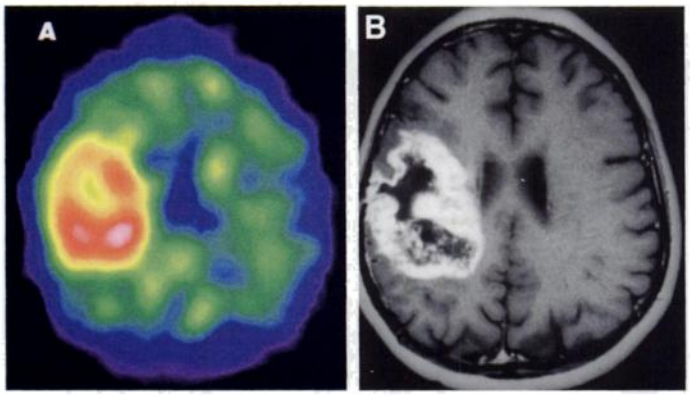

FIGURE 2. Marked IMT uptake in the contrast-enhancing rim of a postsurgical defect (A; transaxial) presented together with the corresponding T1-weighted postgadolinium MRI scan (B) in a patient with recurrence of a glioma IV (Patient 24; IMT uptake ratio = 2.24).